NANO LETTERS

pubs.acs.org/NanoLett Letter

Reversible Thermally Driven Phase Change of Layered In_2Se_3 for Integrated Photonics

Jianghong Wu, Yuting Ye, Jialing Jian, Xiaoping Yao, Junying Li, Bo Tang, Hui Ma, Maoliang Wei, Wenbin Li, Hongtao Lin, and Lan Li*

Cite This: *Nano Lett.* 2023, 23, 6440–6448 Read Online

ACCESS | Metrics & More | Article Recommendations | Supporting Information

ABSTRACT: Two-dimensional In_2Se_3, an unconventional phase-change material, has drawn considerable attention for polymorphic phase transitions and electronic device applications. However, its reversible thermally driven phase transitions and potential use in photonic devices have yet to be explored. In this study, we observe the thermally driven reversible phase transitions between α and β' phases with the assistance of local strain from surface wrinkles and ripples, as well as reversible phase changes within the β phase family. These transitions lead to changes in the refractive index and other optoelectronic properties with minimal optical loss at telecommunication bands, which are crucial in integrated photonic applications such as postfabrication phase trimming. Additionally, multilayer β'-In_2Se_3 working as a transparent microheater proves to be a viable option for efficient thermo-optic modulation. This prototype design for layered In_2Se_3 offers immense potential for integrated photonics and paves the way for multilevel, nonvolatile optical memory applications.

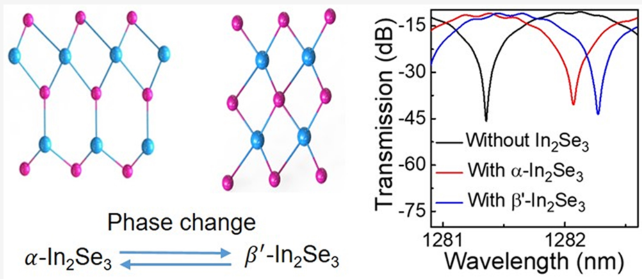

KEYWORDS: *In_2Se_3, optical phase-change material, reversible phase transition, microheater, phase shifter*

Recently, two-dimensional (2D) In_2Se_3 has attracted considerable attention because of the unique properties of its extraordinary ferroelectric, optoelectronic, and thermoelectric properties.[1−7] Intriguingly, In_2Se_3 is polymorphic and possesses multiple crystalline phases, including α, α', β, β', γ, γ', δ, and κ.[8−12] Moreover, the α phase possesses two different stacking sequences, i.e., hexagonal (2H) and rhombohedral (3R) structures, and the β phase possesses three different stacking sequences, i.e., trigonal (1T), 2H, and 3R structures.[9,10] These differences in stacking sequences, the bonding geometries of In/Se atoms, and the vacancy distribution geometries result in different electrical and optical characteristics. For example, α-In_2Se_3 has a noncentrosymmetric crystal structure and both in-plane and out-of-plane ferroelectricity.[13−16] On the contrary, an antiferroelectric order and ferroelasticity were observed in β'-In_2Se_3.[17−19] Indeed, amorphous In_2Se_3 and a part of crystalline phases such as 2H/3R α, 2H/3R β', and γ are stable for 2D In_2Se_3 at room temperature,[20−22] which provides the possibility of multilevel nonvolatile switching. For instance, nonvolatile electronic phase-change memories based on a phase transition from an amorphous to crystalline phase and from a β to a γ phase were realized with the excitation of electric pulses.[20,23,24]

These reported nonvolatile electronic devices primarily rely on the change of conductivity, but the variation of optical characteristics such as refractive index, which plays a significant role in integrated photonics, still needs to be deeply explored. To meet the demand of photonic applications, in-depth studies of optical property changes induced by In_2Se_3 phase change are indispensable. Simultaneously, α-In_2Se_3 and β'-In_2Se_3 possess plentiful physics and material characteristics among all these different phases, but great difficulty still remains for a reversible phase change between these two phases.[22,25,26] Until now, a reversible phase change between β'-In_2Se_3 and α-In_2Se_3 has only been driven by mechanical force.[27] Therefore, finding new approaches for reversible In_2Se_3 phase change and developing nonvolatile integrated photonic devices are meaningful.

Aside from its crystalline polymorphs and compatibility with various phase transition control approaches, In_2Se_3 possesses several advantages over conventional optical phase-change materials in integrated photonics. First, layered In_2Se_3 is back-end CMOS compatible; thereby, it can integrate with arbitrary substrates such as Si and SiN_x for an integrated photonic device, avoiding the technical challenges limited by the variation of lattice constants and thermal expansion coefficients.[28−30] Second, In_2Se_3 has a wide optical bandgap, larger than 1.3 eV,[31,32] bringing about a weak optical absorption and

Received: April 3, 2023
Revised: June 29, 2023
Published: July 5, 2023

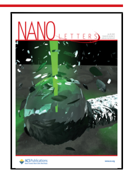

https://doi.org/10.1021/acs.nanolett.3c01247
Nano Lett. 2023, 23, 6440–6448

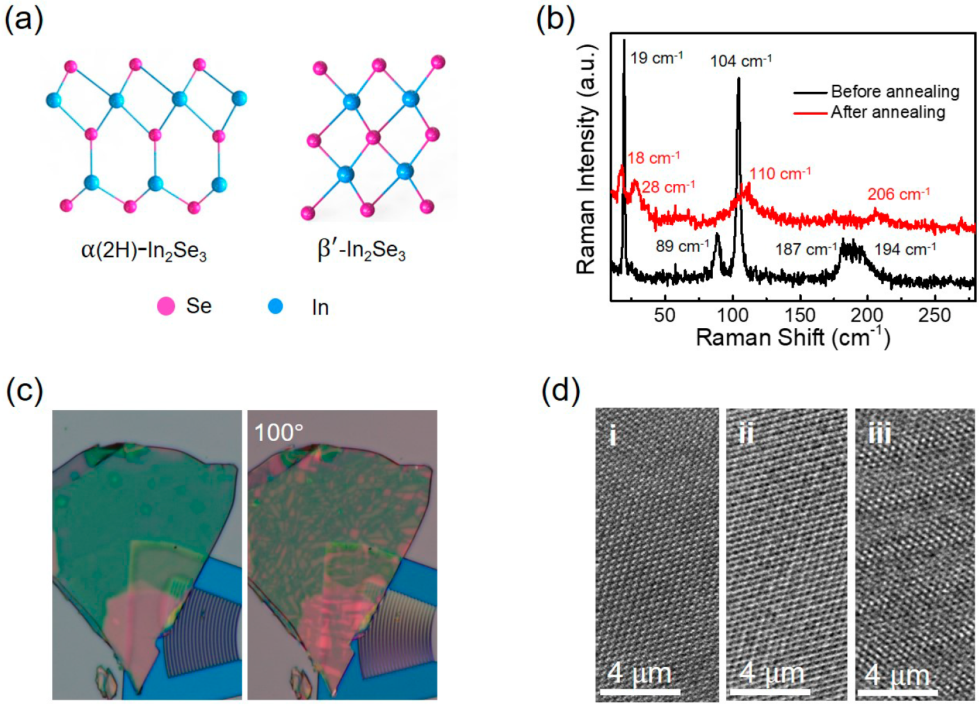

Figure 1. Characterization of multilayer In_2Se_3 flakes before and after annealing. (a) Side-view cartoon of atomic structures for α-In_2Se_3 and β'-In_2Se_3. (b) Raman spectra of a 2H In_2Se_3 flake at 20 °C before (α-In_2Se_3) and after (β'-In_2Se_3) thermal annealing. (c) Optical microscope images of a multilayer In_2Se_3 flake at 20 °C after thermal annealing (β'-In_2Se_3) under nonpolarized light and polarized light (100°). (d) High-resolution transmission electron microscope (TEM) images of a multilayer In_2Se_3 flake at 20 °C (α-In_2Se_3) (i), at 300 °C (β-In_2Se_3) (ii), and at 20 °C after a temperature decrease from 300 °C (β'-In_2Se_3) (iii).

small optical loss at O to U bands. Furthermore, compared with traditional phase-change materials such as $Ge_2Sb_2Te_5$ (melting temperature >650 °C)[33−35] and 2D phase-change materials such as $MoTe_2$ (~900 °C for 2H to 1T′ transition),[36,37] In_2Se_3 possesses a lower phase-change temperature (300 °C @ 50 nm thick) and thus lower power consumption during the phase transition. Therefore, it is valuable to study 2D In_2Se_3 optical property variation and to design phase shifters with low insertion loss based on the phase change of In_2Se_3.

In this work, the reversible phase change of 2H stacked In_2Se_3 between α and β' phases was realized, and the complex phase transitions of multilayer In_2Se_3 and the reversible phase change within the β phase family were also confirmed. This reversible phase change between α and β' phases was induced by a thermal effect with the assistance of local strain from surface wrinkles and ripples. Intriguingly, the phase change between α-In_2Se_3 and β'-In_2Se_3 would result in the variation of refractive index and other optoelectronic properties, which are essential for integrated photonic applications. Benefiting from the phase change, integrated phase shifters based on Mach−Zehnder interferometer (MZI) and microring resonator (MRR) coupling with In_2Se_3 were obtained, which demonstrate the efficient phase modulation and small optical insertion loss (less than 0.012 dB/μm). Moreover, a transparent microheater based on β'-In_2Se_3 was designed for an efficient thermo-optic modulator. The newly discovered heat-induced reversible phase transition in layered In_2Se_3 indicates that it is suitable for low-loss phase trimming and phase modulation and can potentially be used to develop multilevel nonvolatile optical memories under electrical excitation.

The schematic crystal structures of α-In_2Se_3 and β'-In_2Se_3 indicate that they consist of different quintuple Se−In−Se−In−Se layer blocks (Figure 1a). Specifically, 2H α-In_2Se_3 shows the periodical *aBcCa bAcCb* alternate quintuple Se−In−Se−In−Se layers, but β'-In_2Se_3 presents an arrangement in a staggered order of *aBcAb aCbAc* alternating quintuple Se−In−Se−In−Se layers.[9] Raman peaks at 89, 104, 187, and 194 cm^{-1} are observed for a multilayer In_2Se_3 flake (70 nm thick) excited by 532 nm laser at 20 °C (Figure 1b), which are attributed to the E^2, A_1 (LO + TO), A_1 (LO), and A_1 (TO) phonon modes, respectively, and belong to 2H α-In_2Se_3.[10] In the low-frequency region, a Raman peak at 19 cm^{-1} is observed as well. After thermal annealing, the dominant Raman peak has a blue shift to 110 cm^{-1}, and another two emerging peaks at 28 and 206 cm^{-1} belong to the lattice phonon mode of β'-In_2Se_3,[27] indicating the phase change from α to β' phase. An optical microscope image (Figure 1c) of a multilayer In_2Se_3 flake after thermal annealing shows domains in the shape of long stripes under polarized light (100°), resulting from linear-dichroism behavior of β'-In_2Se_3, which indicates that β'-In_2Se_3 comes into being at room temperature after thermal annealing.[18,22] As shown in Figure 1d, high-resolution TEM images taken at different temperatures reveal obvious differences. At 300 °C, the α-In_2Se_3 (i in Figure 1d) flake changes to β-In_2Se_3 (ii in Figure 1d), which only remains at a high temperature and transforms to β'-In_2Se_3 when the temperature decreases from 300 to 20 °C (iii in Figure 1d). Moreover, corresponding selected-area electron diffraction (SAED) patterns are shown in Figure S1 to support the α−β−β' phase change, and Raman spectra at 300 °C (β phase) are illustrated in Figure S2. The structure of β'-In_2Se_3 can be regarded as the parent β-In_2Se_3 structure modified by the

https://doi.org/10.1021/acs.nanolett.3c01247
Nano Lett. 2023, 23, 6440−6448

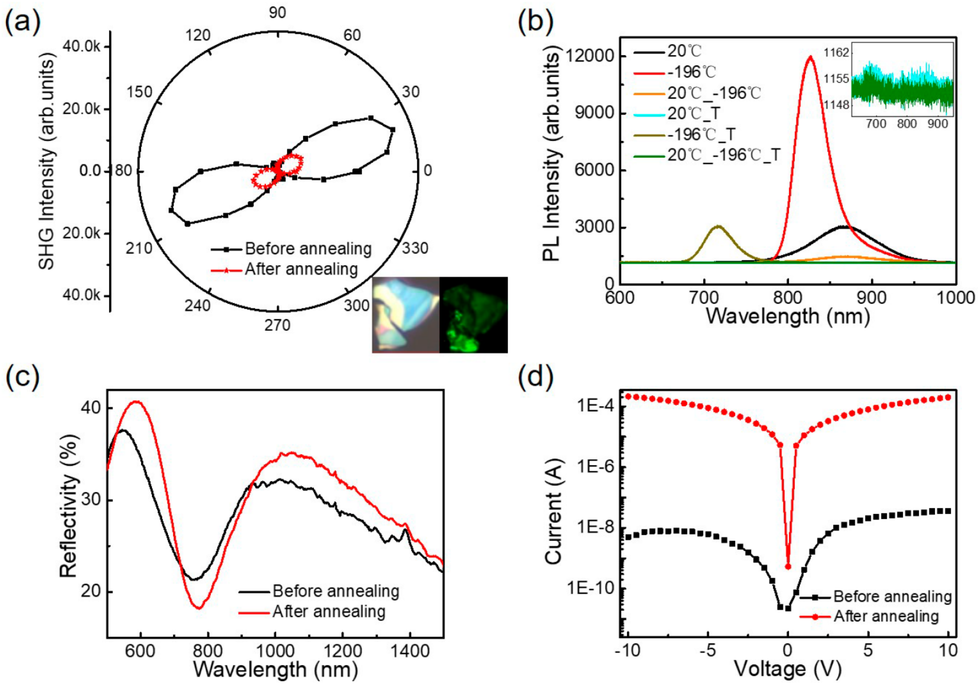

Figure 2. Optoelectronic characteristics variation of flat multilayer In_2Se_3 flakes induced by thermal annealing. (a) The polarization-dependent second-harmonic generation (SHG) of a multilayer In_2Se_3 flake at 20 °C before (α-In_2Se_3) and after (β'-In_2Se_3) thermal annealing. The illustrations in the bottom right corner are an optical microscope image and corresponding SGH mapping. (b) Photoluminescence (PL) spectra of a multilayer In_2Se_3, where T represents the condition of an In_2Se_3 flake after thermal annealing. The inset shows the PL spectra of the In_2Se_3 flake at 20 °C after cooling from 300 °C (β'-In_2Se_3, blue curve) and at 20 °C after cooling from 300 °C and then reverting from −196 °C (β'-In_2Se_3, green curve), respectively. (c) Reflection spectra of a multilayer In_2Se_3 flake before (α-In_2Se_3) and after (β'-In_2Se_3) thermal annealing. (d) Current−voltage curves of a multilayer In_2Se_3 flake before (α-In_2Se_3) and after (β'-In_2Se_3) thermal annealing.

nanostriped superstructure, which was consistent with previous reports.[18] Additionally, thickness reduction occurs along with a phase change from α-In_2Se_3 to β'-In_2Se_3 (Figure S3), which is consistent with the smaller out-of-plane lattice constant c of β'-In_2Se_3 according to a density functional theory (DFT) calculation. In summary, a phase change from 2H α-In_2Se_3 to β'-In_2Se_3 can be realized at 20 °C after thermal annealing.

2H α-In_2Se_3 with broken inversion symmetry possesses strong SHG under the excitation of a picosecond laser at 1064 nm (inset of Figure 2a), with thickness-dependent characteristics, partially resulting from the interference effects between surface and bulk harmonic signals.[38] The polarization-dependent SHG intensity of α-In_2Se_3 shows two-lobe (Figure 2a) and six-lobe (Figure S5) patterns, and the SHG difference can probably be attributed to the changes in In_2Se_3 symmetry and nonlinear photoelasticity induced by local stress.[39−41] Simultaneously, SHG degenerates obviously after thermal annealing at 300 °C, and the weaker SHG belongs to β'-In_2Se_3, which was consistent with the characteristics of in-plane ferroelectricity.[22] Moreover, the polarization-dependent SHG intensity and shape of initial α-In_2Se_3 are different from that of the recovered α-In_2Se_3 (Figure S6), indicating the redistribution of local strain, which is consistent with a morphology change between the initial and recovered α-In_2Se_3 flakes (Figure 3b and Figures S10 and S11). Next, the measured PL spectra of a multilayer 2H α-In_2Se_3 flake under the excitation of a 532 nm laser shows a peak at 869 nm, from which the optical bandgap is inferred to be 1.43 eV at 20 °C. The PL peak has a blue shift to 826 nm at −196 °C, attributed to the reduction of optical bandgap at the lower experimental temperature.[42,43] Meanwhile, the PL peak intensity enhances by 4 times at −196 °C due to the smaller proportion of nonradiative combination, i.e., defect trapping combination and carrier relaxation in the conduction and valence bands at the lower temperature.[44,45] After thermal annealing at 300 °C, the PL signal disappears at 20 °C (the inset in Figure 2b), and a PL peak at 716 nm is observed at −196 °C, whose peak intensity is a fourth of the α-In_2Se_3 counterpart at −196 °C. According to a DFT calculation (Figure 3a), β'-In_2Se_3 is an indirect-bandgap semiconductor; thereby the PL signal at −196 °C may be attributed to the appearance of another distorted β phase, which is consistent with the Raman results in Figure S8. Based on the calculated bandgap and measured PL spectra, it appears that both α-In_2Se_3 and β'-In_2Se_3 exhibit low optical absorption and low insertion loss at the telecommunication band. Furthermore, the reflectivity variation of a multilayer In_2Se_3 flake on the transparent glass substrate is observed because of the In_2Se_3 phase change (Figure 2c), which is induced by thickness reduction and refractive index increase. Moreover, the reflection peaks mainly result from the interference effect of reflexive optical signals at the top and bottom surfaces.

Electrical conductivity variation also occurs as a result of the phase change (Figure 2d). The Au-α-In_2Se_3-Au device (channel length 1.8 μm, thickness 130.2 nm, and width 43.3 μm) shows a Schottky contact, and the current is 36 nA at 10 V. In comparison, the channel current increases to 0.20 mA at 10 V on coming into Ohmic contact after α-In_2Se_3 transforms to β'-In_2Se_3. Although α-In_2Se_3 and β'-In_2Se_3 have almost identical bandgaps according to a DFT calculation (Figure 3a), the channel current of β'-In_2Se_3 is about 4 orders of magnitude larger than that of α-In_2Se_3, primarily resulting from increased mobility and carrier concentration, accompanied by a

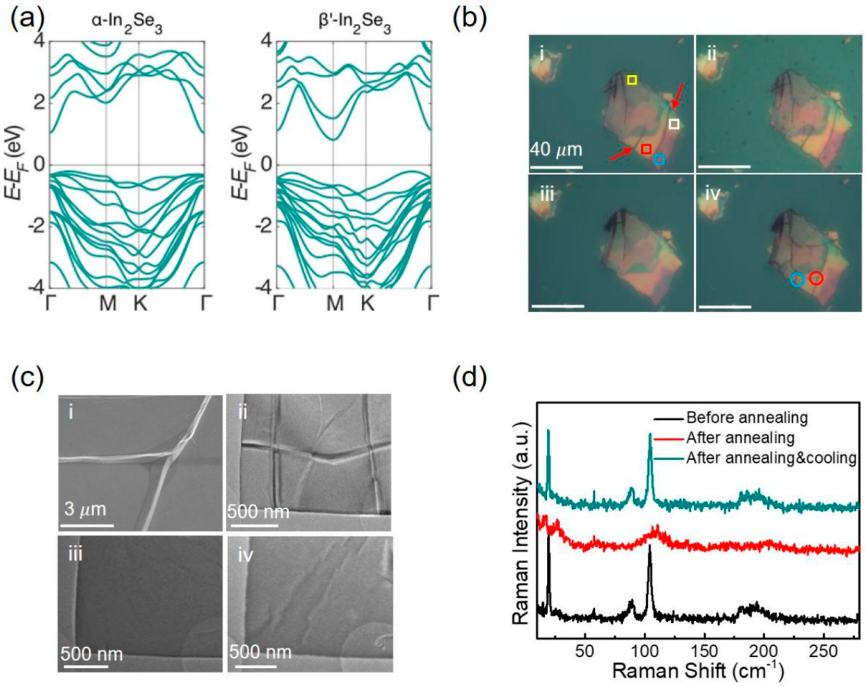

Figure 3. Reversible phase change of wrinkled In_2Se_3 flakes induced by a thermal effect. (a) Calculated band structures for α-In_2Se_3 and β'-In_2Se_3. (b) Optical microscope images of a In_2Se_3 flake at 20 °C (α-In_2Se_3) (i), −196 °C (ii), 20 °C after thermal annealing at 300 °C (β'-In_2Se_3) (iii), and 20 °C after cooling from 300 °C and then reverting from −196 °C (α-In_2Se_3) (iv). Raman spectra at four different square regions were collected (i, Figure 3b). (c) (i) Scanning electron microscope (SEM) image of the In_2Se_3 flake in the region of the red circle (iv in Figure 3b) and in situ TEM images of another wrinkled In_2Se_3 flake at 20 °C (α-In_2Se_3) (ii), 300 °C (β-In_2Se_3) (iii), and 20 °C after cooling from 300 °C (β'-In_2Se_3) (iv). (d) Raman spectra of the multilayer In_2Se_3 flake in the center of the red rectangle (i in Figure 3b). The black, red, and green lines represent the measured Raman signal at 20 °C (α-In_2Se_3), 20 °C after thermal annealing at 300 °C (β'-In_2Se_3), and 20 °C after cooling from 300 °C and then reverting from −196 °C (α-In_2Se_3).

reduction in contact resistance.[8,46] The high electrical conductivity of β'-In_2Se_3 coupled with its large optical bandgap can actually serve as a transparent electrode for thermo-optic modulators with low insertion loss in telecommunication bands.

Thermal effects have complicated impacts on the In_2Se_3 structural variation. Besides the aforementioned α to β' phase change, there are another three types of phase changes induced by thermal effects. First, wrinkles (two black lines marked by red arrows in i in Figure 3b) at the α-In_2Se_3 flake surface disappear after thermal annealing at 300 °C, along with α to β' phase change (iii in Figure 3b). Intriguingly, many more wrinkles and ripples reappear (iv in Figure 3b) at 20 °C after β'-In_2Se_3 recovers from −196 °C, with β'-In_2Se_3 transforming back to α-In_2Se_3. The detailed surface features in the red circle (iv in Figure 3b) are characterized by SEM in Figure 3c (i), demonstrating the obvious wrinkles and ripples instead of cracks on the In_2Se_3 surface. Furthermore, wrinkle disappearance is further observed in the in situ TEM measurement in Figure 3c (ii−iv). After thermal annealing, most of the wrinkles disappear and a nanostriped pattern emerges when the temperature decreases from 300 to 20 °C, corresponding to a phase change from α-In_2Se_3 (ii in Figure 3c) to β-In_2Se_3 (iii in Figure 3c) and to β'-In_2Se_3 (iv in Figure 3c). The variation of surface features during the phase change is attributed to the different lattice constants of α-In_2Se_3 and β'-In_2Se_3. According to a DFT calculation, the in-plane lattice constants a for 2H α-In_2Se_3 and β'-In_2Se_3 are 4.067 and 3.986 and c for 2H α-In_2Se_3 and β'-In_2Se_3 are 19.246 and 18.856, respectively, accounting for the wrinkle variation. This reversible phase change is confirmed by Raman spectra in Figure 3d and Figure S7, indicating that a β'-to-α phase change occurs in the four squares (i in Figure 3b) at 20 °C after reverting from −196 °C. However, the β' phase did not transform to the α phase for those flat In_2Se_3 flakes after reverting from −196 °C (Figure S9). Interestingly, a reversible phase change between the β phase family remained for both wrinkled and flat In_2Se_3 flakes when they were cooled to a temperature lower than −124 °C according to the Raman spectra in Figures S8 and S9. When the temperature decreases from −52 to −124 °C, the Raman peaks at 28 and 110 cm^{-1} will be blue shifted and red shifted, respectively. Simultaneously, another four Raman peaks at 42, 54, 67, and 120 cm^{-1} appear, which probably belong to another distorted β phase.[17] Furthermore, this phase is metastable and it would convert into the β' phase with a temperature increase higher than −124 °C, which is certified by the Raman spectra in Figure S8, providing the possibility for phase transitions at low temperatures. Therefore, we conclude that the wrinkles and ripples in the original α-In_2Se_3 flakes have a significant impact on the heat-induced reversible phase change between β' and α phases. This conclusion is consolidated by another four In_2Se_3 flakes with wrinkles and ripples as shown in Figures S10 and S11, in which the reversible β'-to-α phase change has been observed as well.

Optical phase-change materials with stable and tunable refractive indices are essential for some integrated photonic devices such as nonvolatile phase shifters and postfabrication phase trimming, which play significant roles in photonic applications such as programmable and reconfigurable photonic networks.[47−49] Here, MRRs integrated with multi-

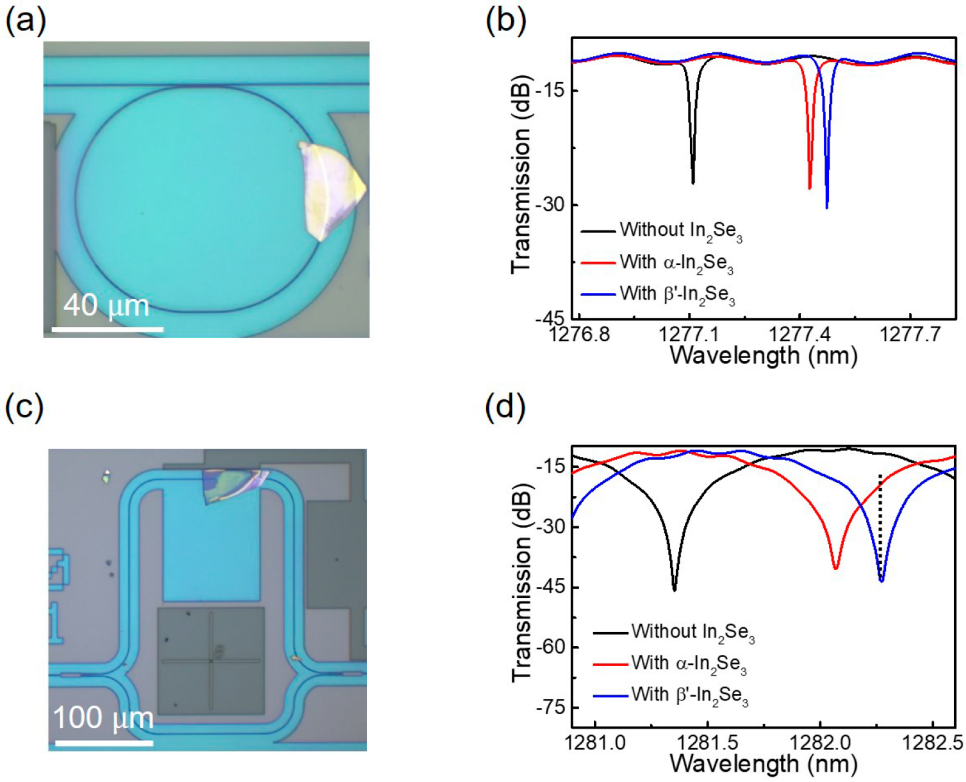

Figure 4. Phase shifter based on the MRR and MZI. (a) Optical microscope image of an MRR integrated with the In_2Se_3 flake (45 nm thick). (b) Transmission spectra of the MRR without and with the In_2Se_3 flake (α and β' phases). (c) Optical microscope image of an MZI integrated with the In_2Se_3 flake (90 nm thick). (d) Transmission spectra of the MZI without and with the In_2Se_3 flake (α and β' phases).

layer In_2Se_3 sheets were designed as phase shifters. We adopted ridge waveguides with a smooth surface on a 220 nm-thick silicon-on-insulator substrate, an etching depth of 150 nm and width of 400 nm, and the detailed fabrication processes are shown in the Supporting Information. An overcoupled race-track MRR integrated with In_2Se_3 was applied to study the resonance variation induced by In_2Se_3 phase change, and the resonance wavelength can be given by

$$n_{ef}L = n_{ef\text{-}In_2Se_3}L_{In_2Se_3} + n_{ef\text{-}Si}L_{Si} = \lambda_{res}m$$

where $n_{ef\text{-}Si}$, $n_{ef\text{-}In_2Se_3}$, $L_{In_2Se_3}$, L_{Si}, and m are the effective refractive index of the Si waveguide, the effective refractive index of the In_2Se_3/Si hybrid waveguide, the length of the In_2Se_3 flake, the circumference length subtracting In_2Se_3 length, and a positive integer, respectively. After transferring a multilayer In_2Se_3 flake (thickness ~45 nm in Figure S14, length 36 μm), the resonance wavelength undergoes a red shift of about 0.317 nm (Figure 4b), and the refractive index of α-In_2Se_3 is calculated to be 2.25 (Figure S13). Meanwhile, the quality factor decreases from 4.2×10^4 to 3.8×10^4, and the ER increases from 16.9 to 17.4 dB at about 1277 nm, which are primarily responsible for the larger scattering loss and the weak defect absorption of the In_2Se_3/Si hybrid waveguide. After thermal annealing at 300 °C, the red shift of resonance wavelength changing from 1277.427 to 1277.470 nm is observed (Figure 4b) due to the phase change of In_2Se_3, and the refractive index of β'-In_2Se_3 is calculated to be 2.47 (Figure S13). Such an obvious refractive index variation plays a prominent role in a nonvolatile phase shifter and post-fabrication phase trimming for integrated photonic applications. Simultaneously, the quality factor increases to 3.9×10^4, resulting from the reduced In_2Se_3 thickness and the smaller optical scattering loss after the phase change. Generally, scattering loss of a 2DM/Si hybrid waveguide is closely related to the volume of 2DM, and In_2Se_3 flakes with thickness ranging from 70 to 120 nm possess low optical loss for the MRR-based phase shifter as shown in Figure S12. Additionally, transmission spectra of two MRRs without In_2Se_3 are shown in Figure S15, in which the almost overlapping spectra indicate that thermal annealing has little impact on the resonance for bare Si MRR.

An unbalanced MZI is another structure for phase shifters that is not limited by channel spacing and grid configuration. Here, MZIs integrated with multilayer α-In_2Se_3 sheets on the longer arm were obtained (Figure 4c). Two 1 × 2 MMIs work as beam splitters and combiners, and the output power can be given by[50,51]

$$P_O = \frac{P_{in}}{4}\left[e^{-\alpha l_1} + e^{-\alpha l_2} + e^{-\alpha(l_1+l_2)/2}\cos\left(2\pi n_{eff}\frac{\Delta L}{\lambda}\right)\right]$$

where P_{in}, α, l_1 and l_2 and ΔL are the input power, the absorption coefficient of the In_2Se_3/Si hybrid waveguide, the lengths of the hybrid waveguide in each arm, and the length difference between the two arms, respectively. Therefore, interference fringes can be obtained when sweeping the input wavelength with an ER expressed by[50]

$$\text{ER} = \frac{P_{max}}{P_{min}} = \frac{e^{-\alpha l_1} + e^{-\alpha l_2} + 2e^{-\alpha(l_1+l_2)/2}}{e^{-\alpha l_1} + e^{-\alpha l_2} - 2e^{-\alpha(l_1+l_2)/2}} = \left(\frac{1 + e^{\alpha \Delta l/2}}{1 - e^{\alpha \Delta l/2}}\right)^2 \approx \left(\frac{4}{\alpha \Delta l}\right)^2$$

https://doi.org/10.1021/acs.nanolett.3c01247
Nano Lett. 2023, 23, 6440−6448

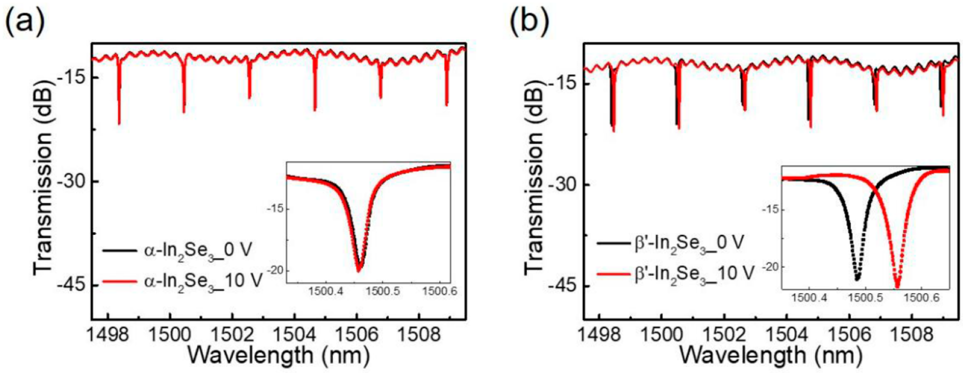

Figure 5. Thermo-optic modulator based on β'-In_2Se_3. Transmission spectra of an MMR with multilayer In_2Se_3 before (a) (α-In_2Se_3) and after (b) (β'-In_2Se_3) thermal annealing under different bias voltages.

where $\Delta l = l_1 - l_2$. As shown in Figure 4d, ER of the original MZI is about 34.1 dB, decreases to 29.5 dB after transferring α-In_2Se_3 (90 nm thick), and then changes to 32.6 dB after thermal annealing. Such a high ER indicates that multilayer In_2Se_3 is a low-loss optical material at the O band, and the absorption coefficients of α-In_2Se_3/Si and β'-In_2Se_3/Si (In_2Se_3: 90 nm thick) hybrid waveguides are inferred to be 0.0113 and 0.0107 dB/μm, respectively, according to the ER variation. A red shift of 206 pm is observed after thermal annealing (Figure 4d) because of the larger refractive index of β'-In_2Se_3, and the on−off ratio is 24.4 dB at 1282.272 nm. In comparison, MZIs without In_2Se_3 possess the same interference fringes after thermal annealing in Figure S15, indicating that this red shift originates from the refractive index variation between α- and β'-In_2Se_3. A shown in Figure S16, the other three MZIs integrated with In_2Se_3 flakes (thickness ranging from 45 to 110 nm) would serve as low-loss phase shifters. Furthermore, a wrinkled α-In_2Se_3 with a reversible phase change between α and β' phases was integrated with MZI (Figure S16f), which demonstrates an obvious variation of transmission spectra when α-In_2Se_3 transformed to β'-In_2Se_3.

A thermo-optic modulator, an important component in integrated photonic circuits, offers the potential for various applications such as optical phased arrays, photonic neural networks, and quantum computation devices.[52−54] Here, multilayer β'-In_2Se_3 possesses a large optical bandgap (Figure 3a) and high conductivity (Figure 2d) accompanied by reduced contact resistance, illustrating the potential to serve as a low-loss microheater for thermo-optic modulators. As shown in Figure 5, the Au-α-In_2Se_3-Au device on top of an MRR shows weak modulation for the resonance wavelengths, limited by the small conductivity. On the contrary, the obvious red shift of resonance wavelength is observed after a phase change from α-In_2Se_3 to β'-In_2Se_3 at 10 V, demonstrating a thermo-optic modulator with small insertion loss. The heating efficiency (η) of this modulator is calculated to be 0.09 nm/mW, which is close to those of thermo-optic modulators based on doped Si[55] and graphene microheaters.[56] Moreover, the half-wave-voltage-length products ($V_\pi L$) at 1500 nm can be approximately calculated to be 0.14 V cm, which is smaller than those of some of the reported modulators based on 2DMs.[57,58]

In summary, we observed thermally driven reversible phase transitions between α and β' phases with the assistance of local strain from surface wrinkles and ripples and confirmed the thermally driven reversible phase transitions within the β phase family. The detailed transition between wrinkled α-In_2Se_3 and β'-In_2Se_3 can be concluded as follows: phase transition from α to β' phase at 20 °C after thermal annealing at 300 °C, a reverted phase transition from β' to α phase at 20 °C after cooling at a temperature below −124 °C, and stability of both 2D α-In_2Se_3 and β'-In_2Se_3 at room temperature. The tunable refractive index induced by a phase change would allow the design of photonic memory devices with low insertion loss and small power consumption, which has been confirmed by the achieved phase shifters with high ER and low insertion loss. Simultaneously, a low-loss thermo-optic modulator based on β'-In_2Se_3 was obtained as well. Overall, this prototype enables layered In_2Se_3 to realize integrated photonic devices for low-loss phase tuning and shows potential applications in nonvolatile optical memory applications.

■ ASSOCIATED CONTENT

Supporting Information

The Supporting Information is available free of charge at https://pubs.acs.org/doi/10.1021/acs.nanolett.3c01247.

Selected-area electron diffraction patterns of In_2Se_3, In_2Se_3 Raman spectra, In_2Se_3 thickness variations after thermal annealing, DFT calculations of the In_2Se_3 unit cell, polarization-dependent second harmonic generation, Raman spectra of the In_2Se_3 flake, phase shifter based on the microring resonator/In_2Se_3, calculated electric field profiles of the TE_0 mode in the hybrid In_2Se_3 waveguide, In_2Se_3 thickness measurement, transmission spectra of Si MRR and unbalanced Mach−Zehnder interferometer (MZI) before and after thermal annealing, and phase shifter based on Mach−Zehnder interferometer/In_2Se_3 (PDF)

■ AUTHOR INFORMATION

Corresponding Author

Lan Li − *Key Laboratory of 3D Micro/Nano Fabrication and Characterization of Zhejiang Province, School of Engineering, Westlake University, Hangzhou 310030, People's Republic of China; Institute of Advanced Technology, Westlake Institute for Advanced Study, Hangzhou 310024, People's Republic of China;* orcid.org/0000-0002-9097-9157; Email: lilan@westlake.edu.cn

Authors

Jianghong Wu − *Key Laboratory of 3D Micro/Nano Fabrication and Characterization of Zhejiang Province,*

School of Engineering, Westlake University, Hangzhou 310030, People's Republic of China; Institute of Advanced Technology, Westlake Institute for Advanced Study, Hangzhou 310024, People's Republic of China
Yuting Ye − *Key Laboratory of 3D Micro/Nano Fabrication and Characterization of Zhejiang Province, School of Engineering, Westlake University, Hangzhou 310030, People's Republic of China; Institute of Advanced Technology, Westlake Institute for Advanced Study, Hangzhou 310024, People's Republic of China*
Jialing Jian − *Key Laboratory of 3D Micro/Nano Fabrication and Characterization of Zhejiang Province, School of Engineering, Westlake University, Hangzhou 310030, People's Republic of China; Institute of Advanced Technology, Westlake Institute for Advanced Study, Hangzhou 310024, People's Republic of China;* orcid.org/0000-0001-6809-6588
Xiaoping Yao − *Key Laboratory of 3D Micro/Nano Fabrication and Characterization of Zhejiang Province, School of Engineering, Westlake University, Hangzhou 310030, People's Republic of China; Institute of Advanced Technology, Westlake Institute for Advanced Study, Hangzhou 310024, People's Republic of China*
Junying Li − *State Key Laboratory of Modern Optical Instrumentation, College of Information Science and Electronic Engineering, Zhejiang University, Hangzhou 310027, People's Republic of China*
Bo Tang − *Institute of Microelectronics, Chinese Academic Society, Beijing 100029, People's Republic of China*
Hui Ma − *State Key Laboratory of Modern Optical Instrumentation, College of Information Science and Electronic Engineering, Zhejiang University, Hangzhou 310027, People's Republic of China*
Maoliang Wei − *State Key Laboratory of Modern Optical Instrumentation, College of Information Science and Electronic Engineering, Zhejiang University, Hangzhou 310027, People's Republic of China*
Wenbin Li − *Key Laboratory of 3D Micro/Nano Fabrication and Characterization of Zhejiang Province, School of Engineering, Westlake University, Hangzhou 310030, People's Republic of China; Institute of Advanced Technology, Westlake Institute for Advanced Study, Hangzhou 310024, People's Republic of China;* orcid.org/0000-0002-1240-2707
Hongtao Lin − *State Key Laboratory of Modern Optical Instrumentation, College of Information Science and Electronic Engineering, Zhejiang University, Hangzhou 310027, People's Republic of China;* orcid.org/0000-0001-7432-3644

Complete contact information is available at:
https://pubs.acs.org/10.1021/acs.nanolett.3c01247

Author Contributions

L.L. and J.W. conceived the project. J.W., Y.Y., J.J., J.L., B.T., H.M., and M.W. fabricated these devices. X.Y. and W.L. conducted the DFT calculation. J.W. performed optical and optoelectronic measurements. L.L, H.L., and J.W. analyzed the data and wrote the manuscript. All authors commented on the manuscript.

Notes

The authors declare no competing financial interest.

■ ACKNOWLEDGMENTS

The authors thank the Westlake Center for Micro/Nano Fabrication and Instrumentation and Service Center for Physical Sciences and Molecular Sciences at Westlake University for the facility support and the ZJU Micro-Nano Fabrication Center at Zhejiang University. We thank Dr. Zhong Chen for Raman measurements and the Westlake HPC Center for technical assistance. The research was partially supported by the National Natural Science Foundation of China (Grant Nos. 12104375, 62175202, 61975179, 91950204, and 62004172), the Leading Innovative and Entrepreneur Team Introduction Program of Zhejiang (2020R01005), and the Zhejiang Provincial Natural Science Foundation of China (LD22F040002).

■ REFERENCES

(1) Si, M.; Saha, A. K.; Gao, S.; Qiu, G.; Qin, J.; Duan, Y.; Jian, J.; Niu, C.; Wang, H.; Wu, W.; et al. A ferroelectric semiconductor field-effect transistor. *Nat. Electron.* **2019**, *2*, 580−586.
(2) Huo, D.; Bai, Y. S.; Lin, X. Y.; Deng, J. H.; Pan, Z. M.; Zhu, C.; Liu, C. S.; Yu, H. Y.; Zhang, C. D. Tuning of the Valley Structures in Monolayer In_2Se_3/WSe_2 Heterostructures via Ferroelectricity. *Nano Lett.* **2022**, *22*, 7261−7267.
(3) Chen, Y. C.; Tang, Z. Y.; Dai, M. Z.; Luo, X.; Zheng, Y. Giant magnetoresistance and tunneling electroresistance in multiferroic tunnel junctions with 2D ferroelectrics. *Nanoscale* **2022**, *14*, 8849−8857.
(4) Nian, T.; Wang, Z.; Dong, B. Thermoelectric properties of α-In_2Se_3 monolayer. *Appl. Phys. Lett.* **2021**, *118*, 033103.
(5) Chen, Y.; Li, D.; Ren, H.; Tang, Y.; Liang, K.; Wang, Y.; Li, F.; Song, C.; Guan, J.; Chen, Z.; et al. Highly Linear and Symmetric Synaptic Memtransistors Based on Polarization Switching in Two-Dimensional Ferroelectric Semiconductors. *Small* **2022**, *18*, 2203611.
(6) Liu, K.; Zhang, T.; Dang, B.; Bao, L.; Xu, L.; Cheng, C.; Yang, Z.; Huang, R.; Yang, Y. An optoelectronic synapse based on α-In_2Se_3 with controllable temporal dynamics for multimode and multiscale reservoir computing. *Nat. Electron.* **2022**, *5*, 761−733.
(7) Li, T.; Wang, Y.; Li, W.; Mao, D.; Benmore, C. J.; Xing, H.; Li, Q.; Wang, F.; Sivaraman, G.; Janotti, A.; et al. Structure phase transition in layered materials for integrated photonic memory. *Adv. Mater.* **2022**, *34*, 2108261.
(8) Li, J.; Li, H.; Niu, X.; Wang, Z. Low-Dimensional In_2Se_3 Compounds: From Material Preparations to Device Applications. *ACS Nano* **2021**, *15*, 18683−18707.
(9) Liu, L.; Dong, J.; Huang, J.; Nie, A.; Zhai, K.; Xiang, J.; Wang, B.; Wen, F.; Mu, C.; Zhao, Z.; et al. Atomically resolving polymorphs and crystal structures of In_2Se_3. *Chem. Mater.* **2019**, *31*, 10143−10149.
(10) KüPers, M.; Konze, P. M.; Meledin, A.; Mayer, J.; Englert, U.; Wuttig, M.; Dronskowski, R. Controlled crystal growth of indium selenide, In_2Se_3, and the crystal structures of α-In_2Se_3. *Inorg. Chem.* **2018**, *57*, 11775−11781.
(11) Van Landuyt, J.; Van Tendeloo, G.; Amelinckx, S. Phase transitions in In_2Se_3 as studied by electron microscopy and electron diffraction. *Phys. Status Solidi A* **1975**, *30*, 299−314.
(12) Li, W.; Sabino, F. P.; de Lima, F. C.; Wang, T.; Miwa, R. H.; Janotti, A. Large disparity between optical and fundamental band gaps in layered In_2Se_3. *Phys. Rev. B* **2018**, *98*, 165134.
(13) Su, Y. R.; Li, X. L.; Zhu, M.; Zhang, J.; You, L.; Tsymbal, E. Y. Van der Waals Multiferroic Tunnel Junctions. *Nano Lett.* **2021**, *21*, 175−181.
(14) Xiao, J.; Zhu, H.; Wang, Y.; Feng, W.; Hu, Y.; Dasgupta, A.; Han, Y.; Wang, Y.; Muller, D. A.; Martin, L. W.; et al. Intrinsic two-dimensional ferroelectricity with dipole locking. *Phys. Rev. Lett.* **2018**, *120*, 227601.
(15) Ding, W.; Zhu, J.; Wang, Z.; Gao, Y.; Xiao, D.; Gu, Y.; Zhang, Z.; Zhu, W. Prediction of intrinsic two-dimensional ferroelectrics in

In_2Se_3 and other III_2-VI_3 van der Waals materials. *Nat. Commun.* **2017**, *8*, 14956.
(16) Huang, K.; Shao, D.-F.; Tsymbal, E. Y. Ferroelectric Control of Magnetic Skyrmions in Two-Dimensional van der Waals Heterostructures. *Nano Lett.* **2022**, *22*, 3349−3355.
(17) Zhang, Z.; Nie, J.; Zhang, Z.; Yuan, Y.; Fu, Y. S.; Zhang, W. Atomic Visualization and Switching of Ferroelectric Order in β-In_2Se_3 Films at the Single Layer Limit. *Adv. Mater.* **2022**, *34*, 2106951.
(18) Xu, C.; Mao, J.; Guo, X.; Yan, S.; Chen, Y.; Lo, T. W.; Chen, C.; Lei, D.; Luo, X.; Hao, J.; et al. Two-dimensional ferroelasticity in van der Waals β'-In_2Se_3. *Nat. Commun.* **2021**, *12*, 3665.
(19) Wu, Z.; Liu, K.; Mu, X.; Zhou, J. Renormalizing Antiferroelectric Nanostripes in β'-In2Se3 via Optomechanics. *J. Phys. Chem. Lett.* **2023**, *14*, 677−684.
(20) Choi, M. S.; Cheong, B. k.; Ra, C. H.; Lee, S.; Bae, J. H.; Lee, S.; Lee, G. D.; Yang, C. W.; Hone, J.; Yoo, W. J. Electrically driven reversible phase changes in layered In_2Se_3 crystalline film. *Adv. Mater.* **2017**, *29*, 1703568.
(21) Ho, C.-H.; Chen, Y.-C.; Pan, C.-C. Structural phase transition and erasable optically memorized effect in layered γ-In_2Se_3 crystals. *J. Appl. Phys.* **2014**, *115*, 033501.
(22) Zheng, C.; Yu, L.; Zhu, L.; Collins, J. L.; Kim, D.; Lou, Y.; Xu, C.; Li, M.; Wei, Z.; Zhang, Y.; et al. Room temperature in-plane ferroelectricity in van der Waals In_2Se_3. *Sci. Adv.* **2018**, *4*, No. eaar7720.
(23) Yu, B.; Ju, S.; Sun, X.; Ng, G.; Nguyen, T. D.; Meyyappan, M.; Janes, D. B. Indium selenide nanowire phase-change memory. *Appl. Phys. Lett.* **2007**, *91*, 133119.
(24) Lee, H.; Kang, D.-H.; Tran, L. Indium selenide (In_2Se_3) thin film for phase-change memory. *Mater. Sci. Engineering: B* **2005**, *119*, 196−201.
(25) Tao, X.; Gu, Y. Crystalline-crystalline phase transformation in two-dimensional In_2Se_3 thin layers. *Nano Lett.* **2013**, *13*, 3501−3505.
(26) Lyu, F.; Li, X.; Tian, J.; Li, Z.; Liu, B.; Chen, Q. Temperature-Driven α-β Phase Transformation and Enhanced Electronic Property of 2H α-In_2Se_3. *ACS Appl. Mater. Interfaces* **2022**, *14*, 23637−23644.
(27) Han, W.; Zheng, X.; Yang, K.; Tsang, C. S.; Zheng, F.; Wong, L. W.; Lai, K. H.; Yang, T.; Wei, Q.; Li, M.; et al. Phase-controllable large-area two-dimensional In_2Se_3 and ferroelectric heterophase junction. *Nat. Nanotechnol.* **2023**, *18*, 55−63.
(28) Ma, Y.; Chang, Y.; Dong, B.; Wei, J.; Liu, W.; Lee, C. Heterogeneously integrated graphene/silicon/halide waveguide photodetectors toward chip-scale zero-bias long-wave infrared spectroscopic sensing. *ACS Nano* **2021**, *15*, 10084−10094.
(29) Wu, J.; Ma, H.; Zhong, C.; Wei, M.; Sun, C.; Ye, Y.; Xu, Y.; Tang, B.; Luo, Y.; Sun, B.; Jian, J.; Dai, H.; Lin, H.; Li, L. Waveguide-Integrated $PdSe_2$ Photodetector over a Broad Infrared Wavelength Range. *Nano Lett.* **2022**, *22*, 6816−6824.
(30) Wang, Y.; Pelgrin, V.; Gyger, S.; Uddin, G. M.; Bai, X.; Lafforgue, C.; Vivien, L.; Jöns, K. D.; Cassan, E.; Sun, Z. Enhancing Si_3N_4 waveguide nonlinearity with heterogeneous integration of few-layer WS_2. *ACS Photonics* **2021**, *8*, 2713−2721.
(31) Almeida, G.; Dogan, S.; Bertoni, G.; Giannini, C.; Gaspari, R.; Perissinotto, S.; Krahne, R.; Ghosh, S.; Manna, L. Colloidal monolayer β-In_2Se_3 nanosheets with high photoresponsivity. *J. Am. Chem. Soc.* **2017**, *139*, 3005−3011.
(32) Quereda, J.; Biele, R.; Rubio-Bollinger, G.; Agraït, N.; D'Agosta, R.; Castellanos-Gomez, A. Strong quantum confinement effect in the optical properties of ultrathin α-In_2Se_3. *Adv. Opt. Mater.* **2016**, *4*, 1939−1943.
(33) Kato, T.; Tanaka, K. Electronic properties of amorphous and crystalline $Ge_2Sb_2Te_5$ films. *Jpn. J. Appl. Phys.* **2005**, *44*, 7340.
(34) Zheng, J.; Zhu, S.; Xu, P.; Dunham, S.; Majumdar, A. Modeling Electrical Switching of Nonvolatile Phase-Change Integrated Nanophotonic Structures with Graphene Heaters. *ACS Appl. Mater. Interfaces* **2020**, *12*, 21827−21836.
(35) Chen, R.; Fang, Z.; Miller, F.; Rarick, H.; Froch, J. E.; Majumdar, A. Opportunities and Challenges for Large-Scale Phase-Change Material Integrated Electro-Photonics. *ACS Photonics* **2022**, *9*, 3181−3195.
(36) Sengupta, R.; Dangi, S.; Krylyuk, S.; Davydov, A. V.; Pavlidis, S. Phase transition of Al_2O_3-encapsulated $MoTe_2$ via rapid thermal annealing. *Appl. Phys. Lett.* **2022**, *121*, 033101.
(37) Wang, Y.; Zhang, M.; Xue, Z.; Chen, X.; Mei, Y.; Chu, P. K.; Tian, Z.; Wu, X.; Di, Z. Atomistic observation of the local phase transition in $MoTe_2$ for application in homojunction photodetectors. *Small* **2022**, *18*, 2200913.
(38) Deckoff-Jones, S.; Zhang, J.; Petoukhoff, C. E.; Man, M. K.; Lei, S.; Vajtai, R.; Ajayan, P. M.; Talbayev, D.; Madéo, J.; Dani, K. M. Observing the interplay between surface and bulk optical nonlinearities in thin van der Waals crystals. *Sci. Rep.* **2016**, *6*, 35705.
(39) Cho, Y.; Anderson, S. M.; Mendoza, B. S.; Okano, S.; Arzate, N.; Shkrebtii, A. I.; Wu, D.; Lai, K.; Carriles, R.; Zahn, D.; et al. Second-harmonic and linear spectroscopy of α-In_2Se_3. *Phys. Rev. Mater.* **2022**, *6*, 034006.
(40) Liang, J.; Zhang, J.; Li, Z.; Hong, H.; Wang, J.; Zhang, Z.; Zhou, X.; Qiao, R.; Xu, J.; Gao, P.; et al. Monitoring local strain vector in atomic-layered $MoSe_2$ by second-harmonic generation. *Nano Lett.* **2017**, *17*, 7539−7543.
(41) Mennel, L.; Paur, M.; Mueller, T. Second harmonic generation in strained transition metal dichalcogenide monolayers: MoS_2, $MoSe_2$, WS_2, and WSe_2. *APL Photonics* **2019**, *4*, 034404.
(42) Varshni, Y. P. Temperature dependence of the energy gap in semiconductors. *physica* **1967**, *34*, 149−154.
(43) Korn, T.; Heydrich, S.; Hirmer, M.; Schmutzler, J.; Schüller, C. Low-temperature photocarrier dynamics in monolayer MoS_2. *Appl. Phys. Lett.* **2011**, *99*, 102109.
(44) Nan, H.; Wang, Z.; Wang, W.; Liang, Z.; Lu, Y.; Chen, Q.; He, D.; Tan, P.; Miao, F.; Wang, X.; et al. Strong photoluminescence enhancement of MoS_2 through defect engineering and oxygen bonding. *ACS Nano* **2014**, *8*, 5738−5745.
(45) Ugeda, M. M.; Bradley, A. J.; Shi, S.-F.; Da Jornada, F. H.; Zhang, Y.; Qiu, D. Y.; Ruan, W.; Mo, S.-K.; Hussain, Z.; Shen, Z.-X. Giant bandgap renormalization and excitonic effects in a monolayer transition metal dichalcogenide semiconductor. *Nat. Mater.* **2014**, *13*, 1091−1095.
(46) Feng, W.; Gao, F.; Hu, Y.; Dai, M.; Liu, H.; Wang, L.; Hu, P. Phase-Engineering-Driven Enhanced Electronic and Optoelectronic Performance of Multilayer In_2Se_3 Nanosheets. *ACS Appl. Mater. Interfaces* **2018**, *10*, 27584−27588.
(47) Bogaerts, W.; Pérez, D.; Capmany, J.; Miller, D. A.; Poon, J.; Englund, D.; Morichetti, F.; Melloni, A. Programmable photonic circuits. *Nature* **2020**, *586*, 207−216.
(48) Ceccarelli, F.; Atzeni, S.; Prencipe, A.; Farinaro, R.; Osellame, R. Thermal phase shifters for femtosecond laser written photonic integrated circuits. *J. Lightwave Technol.* **2019**, *37*, 4275−4281.
(49) Chen, X.; Milosevic, M. M.; Thomson, D. J.; Khokhar, A. Z.; Franz, Y.; Runge, A. F.; Mailis, S.; Peacock, A. C.; Reed, G. T. Post-fabrication phase trimming of Mach-Zehnder interferometers by laser annealing of germanium implanted waveguides. *Photonics Res.* **2017**, *5*, 578−582.
(50) Li, H.; Anugrah, Y.; Koester, S. J.; Li, M. Optical absorption in graphene integrated on silicon waveguides. *Appl. Phys. Lett.* **2012**, *101*, 111110.
(51) Lin, H. T.; Song, Y.; Huang, Y. Z.; Kita, D.; Deckoff-Jones, S.; Wang, K. Q.; Li, L.; Li, J. Y.; Zheng, H. Y.; Luo, Z. Q.; Wang, H. Z.; Novak, S.; Yadav, A.; Huang, C. C.; Shiue, R. J.; Englund, D.; Gu, T.; Hewak, D.; Richardson, K.; Kong, J.; Hu, J. J. Chalcogenide glass-on-graphene photonics. *Nat. Photonics* **2017**, *11*, 798−805.
(52) Chung, S.; Abediasl, H.; Hashemi, H. A monolithically integrated large-scale optical phased array in silicon-on-insulator CMOS. *IEEE J. Solid-St. Circ.* **2018**, *53*, 275−296.
(53) Liu, S.; Feng, J.; Tian, Y.; Zhao, H.; Jin, L.; Ouyang, B.; Zhu, J.; Guo, J. Thermo-optic phase shifters based on silicon-on-insulator platform: State-of-the-art and a review. *Frontiers of Optoelectronics* **2022**, *15*, 9.

(54) Harris, N. C.; Steinbrecher, G. R.; Prabhu, M.; Lahini, Y.; Mower, J.; Bunandar, D.; Chen, C.; Wong, F. N.; Baehr-Jones, T.; Hochberg, M.; et al. Quantum transport simulations in a programmable nanophotonic processor. *Nat. Photonics* **2017**, *11*, 447−452.

(55) Zhong, C.; Ma, H.; Sun, C.; Wei, M.; Ye, Y.; Tang, B.; Zhang, P.; Liu, R.; Li, J.; Li, L.; et al. Fast thermo-optical modulators with doped-silicon heaters operating at 2 μm. *Opt. Express* **2021**, *29*, 23508−23516.

(56) Zhong, C.; Zhang, Z.; Ma, H.; Wei, M.; Ye, Y.; Wu, J.; Tang, B.; Zhang, P.; Liu, R.; Li, J.; et al. Silicon Thermo-Optic Switches with Graphene Heaters Operating at Mid-Infrared Waveband. *Nanomaterials* **2022**, *12*, 1083.

(57) Sorianello, V.; Midrio, M.; Contestabile, G.; Asselberghs, I.; Van Campenhout, J.; Huyghebaert, C.; Goykhman, I.; Ott, A.; Ferrari, A.; Romagnoli, M. Graphene-silicon phase modulators with gigahertz bandwidth. *Nat. Photonics* **2018**, *12*, 40−44.

(58) Datta, I.; Chae, S. H.; Bhatt, G. R.; Tadayon, M. A.; Li, B.; Yu, Y.; Park, C.; Park, J.; Cao, L.; Basov, D.; et al. Low-loss composite photonic platform based on 2D semiconductor monolayers. *Nat. Photonics* **2020**, *14*, 256−262.

https://doi.org/10.1021/acs.nanolett.3c01247
Nano Lett. 2023, 23, 6440−6448